RSC Advances

PAPER

View Article Online
View Journal | View Issue

Cite this: *RSC Adv.*, 2025, **15**, 30564

Upcycling battery waste into Zn-BTC metal organic framework for dual applications in electrochemical sensing of uric acid and antibacterial applications

Md Sohag Hossain, [a] Sharuk Alam Aumi,[b] Nourin Tarannum,[c] Fariha Chowdhury, [d] Md. Sahadat Hossain, [a] Md. Farid Ahmed,[a] Nazmul Islam Tanvir,[e] Umme Sarmeen Akhtar,[a] Samina Ahmed *[a] and Mashrafi Bin Mobarak *[a]

This study reports the sustainable synthesis of a zinc-based metal–organic framework (Zn-BTC MOF) using zinc, extracted from waste dry cell batteries. A three-step route involving zinc recovery, hydroxide precipitation, and solvothermal coordination with 1,3,5-benzenetricarboxylic acid (BTC) led to the formation of crystalline Zn-BTC. Comprehensive characterization, utilizing techniques such as XRD, FTIR, Raman, FESEM, TEM, XPS, EDS, and TGA-DSC, confirmed the formation of a highly ordered Zn-BTC MOF framework structure with nanoscale morphology and thermal stability. Zn-BTC MOF exhibited promising electrochemical performance in detecting uric acid (UA), with a wide linear detection range (0–200 μM), low detection limit (1.43 μM), and high electroactive surface area (0.16 cm^2). Additionally, the MOF showed significant antibacterial activity, with minimum inhibitory and bactericidal concentrations of 0.1 and 0.6 mg mL^{-1} against *Bacillus subtilis*, and 0.2 and 0.8 mg mL^{-1} against *Escherichia coli*. By fabricating the MOF using recycled zinc, this research highlights its dual potential as a high-performance electrochemical sensor and antibacterial agent.

Received 9th July 2025
Accepted 14th August 2025

DOI: 10.1039/d5ra04903b

rsc.li/rsc-advances

1. Introduction

Uric acid (UA) is a key end-product of purine metabolism in humans and is commonly found in blood and urine.[1] Although UA functions as an antioxidant at normal levels, its accumulation is linked to serious health issues such as hyperuricemia, gout, cardiovascular disease, kidney dysfunction, and metabolic syndrome.[1–4] Therefore, reliable, rapid, and sensitive detection of UA is of great clinical importance for the early diagnosis and monitoring of related disorders.[5,6]

A variety of analytical techniques such as high-performance liquid chromatography (HPLC),[7] capillary electrophoresis,[8] chemiluminescence,[9] spectrophotometry,[10] and enzymatic assays[11] have been utilized for UA detection. However, these methods often suffer from limitations including high cost, time-consuming sample preparation, complex instrumentation, and poor portability. In contrast, electrochemical techniques offer attractive alternatives due to their simplicity, rapid response, cost-effectiveness, high sensitivity, and ability to operate in real biological environments.[12,13] However, the performance of electrochemical sensors largely depends on the properties of the electrode-modifying materials, which must provide high surface area, abundant active sites, and efficient electron transfer pathways.[14]

To address these requirements, researchers have increasingly turned to advanced functional materials, with metal–organic frameworks (MOFs) attracting significant interest.[15] MOFs combine metal centers with organic linkers to create highly porous structures that enhance analyte adsorption and electron transfer, thereby improving electrocatalytic performance.[16] Within various types of MOFs, zinc-based MOFs (Zn-MOFs) are particularly gaining interest because of their redox activity, environmental stability, and biocompatibility, making them suitable for biosensing and biomedical applications.[17]

Zn-MOFs have been effectively employed for the electrochemical sensing of various analytes including UA.[18] In particular, Zn-based MOFs have shown excellent performance in UA detection due to their high density of redox-active Zn^{2+} sites, tunable pore structures, and ability to facilitate both adsorption and electron transfer, which collectively enhance sensitivity and selectivity.[19] These frameworks have also demonstrated antimicrobial activity due to the gradual release of Zn^{2+} ions, which

[a]*Institute of Glass and Ceramic Research and Testing (IGCRT), Bangladesh Council of Scientific and Industrial Research (BCSIR), Dhaka-1205, Bangladesh. E-mail: shanta_samina@yahoo.com; mashrafibinmobarak@gmail.com*

[b]*Department of Chemistry, University of Dhaka, Dhaka- 1000, Bangladesh*

[c]*Institute of Technology Transfer and Innovation (ITTI), Bangladesh Council of Scientific and Industrial Research (BCSIR), Dhaka-1205, Bangladesh*

[d]*Biomedical and Toxicological Research Institute (BTRI), Bangladesh Council of Scientific and Industrial Research (BCSIR), Dhaka-1205, Bangladesh*

[e]*BCSIR Dhaka Laboratories, Bangladesh Council of Scientific and Industrial Research (BCSIR), Dhaka-1205, Bangladesh*

interfere with bacterial membrane integrity and enzyme function.[20,21] Despite these advances, many synthesis routes for MOFs rely on commercially available metal salts, which can be expensive and environmentally taxing.

With growing interest in sustainable materials development, there is a pressing need to adopt green strategies for MOF synthesis.[22] Recycling valuable metals from electronic waste, such as zinc from spent dry cell batteries, offers an effective solution to reducing environmental impact while providing a low-cost precursor for MOF fabrication. In this study, we demonstrate the extraction of metallic zinc from discarded dry cells and its use in the synthesis of a Zn-BTC MOF using 1,3,5-benzenetricarboxylic acid (BTC) as an organic linker.

The synthesized Zn-BTC MOF was characterized using multiple analytical techniques including X-ray diffraction (XRD), Fourier-transform infrared (FTIR) spectroscopy, Raman spectroscopy, field emission scanning electron microscopy (FESEM), transmission electron microscopy (TEM), X-ray photoelectron spectroscopy (XPS), energy-dispersive X-ray spectroscopy (EDS), and simultaneous thermal analysis (TG-DSC). The material was subsequently evaluated for its electrochemical performance toward UA, an important biomarker linked to metabolic disorders. Additionally, its antibacterial activity was tested against both Gram-positive (*Bacillus subtilis*) and Gram-negative (*Escherichia coli*) bacteria, further extending its relevance in biomedical and environmental applications. This work aims to bridge sustainable materials science and practical functionality, offering a pathway toward circular economy practices through value-added MOF production from battery waste.

2. Materials and method

2.1. Materials

All the chemicals used in this research were of analytical grade and used without further purification. BTC (extra pure, 98%) was obtained from Sisco Research Laboratories Private Limited (India). *N*,*N*-Dimethylformamide (DMF) and ethanol (C_2H_6O) were purchased from Merck Life Science Private Limited (India) and Merck KGaA (Germany), respectively. Triethylamine ($(C_2H_5)_3N$), hydrochloric acid (HCl, 37%), and uric acid ($C_5H_4N_4O_3$) were supplied by Sigma-Aldrich (Germany). Sodium hydroxide (NaOH), sodium dihydrogen phosphate (NaH_2PO_4), disodium hydrogen phosphate (Na_2HPO_4), and silver nitrate ($AgNO_3$) were also sourced from Merck KGaA. For antibacterial studies, Gram-positive *Bacillus subtilis* (ATCC 6633) and Gram-negative *Escherichia coli* (ATCC 11229) were used as test organisms. All experimental procedures were carried out using deionized (DI) water with a resistivity of 18.2 MΩ cm.

2.2. Synthesis of Zn-BTC MOF

2.2.1. Extraction of zinc from waste dry cells. Zinc metal was collected from used dry cell batteries and utilized as the starting material for Zn-BTC MOF synthesis. The discarded batteries were first opened manually using pliers. The outer steel cover was carefully removed to access the inner zinc shell. A black powdery substance, primarily made up of manganese dioxide (MnO_2) and graphite, was present along with a carbon rod in the centre. These materials were separated by hand, leaving behind the Zn shell. The Zn shell was then washed several times with distilled water to remove the loose black powder. To ensure a clean surface free of residual particles, the zinc shell was scrubbed with sandpaper. This step removed oxide layers, enhancing the reactivity of the surface. After cleaning, the Zn was left to dry at room temperature.

2.2.2. Preparation of zinc hydroxide ($Zn(OH)_2$). The extracted Zn (3.0 g) was dissolved in 50 mL of 10% HCl solution under continuous stirring at 50 °C until a clear $ZnCl_2$ solution was obtained. To this, 50 mL of 1 M NaOH was added dropwise with continuous stirring, leading to the formation of a white gelatinous precipitate of $Zn(OH)_2$. NaOH was further added until the pH reached 9, followed by an additional 10 minutes of stirring to ensure complete precipitation. The precipitate was then filtered and thoroughly washed with DI water to remove residual chloride ions. The absence of chloride was confirmed using $AgNO_3$ solution (no white precipitate formation). The purified zinc hydroxide was dried in a hot air oven at 80 °C for 8 hours, yielding 3.95 g of $Zn(OH)_2$.

2.2.3. Synthesis of Zn-BTC MOF. To synthesize Zn-BTC, 1.485 g of $Zn(OH)_2$ (0.015 mol) was first dissolved in 15 mL of 10% nitric acid (HNO_3) under stirring to ensure complete dissolution of the hydroxide. Separately, 2.1014 g of BTC (0.01 mol) was dispersed in a mixture of DMF, and ethanol (15 mL each; total 30 mL) in a Duran bottle. The $Zn(NO_3)_2$ solution was then added to this ligand-containing mixture. To promote deprotonation of the carboxylic acid groups and enhance coordination, 2 mL of triethylamine was introduced into the reaction mixture. The sealed vessel was heated in an oven at 100 °C for 24 hours under solvothermal conditions. After the reaction, white crystalline Zn-BTC MOF was observed settled at the bottom of the bottle. The mixture was allowed to cool to room temperature, and the supernatant was decanted. The solid product was then washed thoroughly with DMF, deionized water, and ethanol to remove unreacted precursors and solvents. Finally, the crystals were air-dried at room temperature for 24 hours and ground into a fine powder. The total yield of Zn-BTC MOF was 1.3269 g, corresponding to an approximate percentage yield of 40.70% based on the amount of $Zn(OH)_2$ used.

2.3. Characterization techniques

The structural and morphological properties of the synthesized Zn-BTC were characterized using various analytical tools. X-ray diffraction (XRD) patterns were recorded with a Rigaku SmartLab diffractometer using Cu-Kα radiation ($\lambda = 1.5406$ Å) in out-of-plane geometry. Functional groups and bonding characteristics were analyzed using Fourier-transform infrared (FTIR) and Raman spectroscopy. FTIR spectra were obtained on a Shimadzu IR Prestige21 spectrometer with an ATR accessory over the range of 4000–400 cm^{-1}, averaging 30 scans at 4 cm^{-1} resolution. Raman measurements were performed using a Horiba MacroRam spectrometer with a 785 nm laser,

calibrated using a standard silicon band at ~520 cm^{-1}. Morphology was examined by field emission scanning electron microscopy (FESEM) on a JEOL JSM-7610F and transmission electron microscopy (TEM) using a Talos F200X G2. Samples for FESEM were platinum-coated, while TEM grids were prepared by drop-casting ethanol-dispersed powders onto carbon-coated copper grids. Elemental composition was determined *via* energy-dispersive X-ray spectroscopy (EDS) attached to the FESEM, using a 1 nA probe current and ZAF correction for quantification. X-ray photoelectron spectroscopy (XPS) analysis was carried out using a Thermo Scientific K-ALPHA system with Al Kα radiation, under ultra-high vacuum. Surface cleaning was done using low-energy ion beam etching prior to measurement. Thermal properties were examined using a simultaneous thermal analyzer (STA) (NETZSCH STA 449 F5), operating at a heating rate of 10 K min^{-1} under a continuous nitrogen gas flow.

2.4. Electrochemical measurements

The electrochemical properties of the synthesized Zn-BTC MOF were investigated using a conventional three-electrode system connected to an electrochemical workstation (CH Instruments, CHI650E). A glassy carbon electrode (GCE, 3 mm diameter) modified with Zn-BTC MOF served as the working electrode, while a platinum wire and Ag/AgCl (3 M KCl) were used as the counter and reference electrodes, respectively. Prior to modification, the GCE was polished with 0.3- and 0.5-micron alumina powder, rinsed thoroughly with DI water, and dried under nitrogen. The Zn-BTC MOF suspension (1 mg mL^{-1} in DI water) was ultrasonicated for uniform dispersion, and ~7.5 μL of this suspension was drop-casted onto the GCE surface and air-dried at room temperature.

All electrochemical measurements were performed in phosphate-buffered saline (PBS, 0.1 M, pH 7.4) at room temperature. Cyclic voltammetry (CV) was conducted over a potential range of −0.5 V to +1.0 V at scan rates ranging from 10 to 100 mV s^{-1} to evaluate the redox behaviour and scan rate dependence of UA. The sensitivity of the modified electrode was examined by recording CVs at increasing concentrations of UA (0–300 μM). Calibration curves were constructed from anodic peak currents as a function of UA concentration to assess the sensor's linear range and sensitivity. For kinetic analysis, the peak currents were plotted against the scan rate (ν) and the square root of the scan rate ($\nu^{1/2}$) to determine whether the process was adsorption-controlled or diffusion-controlled. All measurements were repeated three times to ensure reproducibility and stability of the sensor response.

2.5. Antibacterial activity evaluation

2.5.1. Agar well diffusion assay. The antibacterial activity of Zn-BTC MOF was evaluated using the standard agar well diffusion method as described in previous studies.[23,24] Sterile Mueller-Hinton Agar (MHA) (20–25 mL) was poured into 90 mm Petri dishes and allowed to solidify under aseptic conditions. A freshly prepared bacterial suspension (approx. 10^5 CFU mL^{-1}, OD_{600} = 0.05) was uniformly spread onto the solidified agar surface using a sterile cotton swab. Sterile 6 mm wells were punched into the agar using a cork borer. A volume of 100 μL of Zn-BTC MOF solutions at various concentrations (0.1, 0.2, 0.3, 0.4, and 0.5 mg mL^{-1}) was carefully pipetted into each well. A tetracycline disc was used as a positive control, while dimethyl sulfoxide (DMSO) served as the negative control. The inoculated plates were incubated at 37 °C for 24 hours, after which the zones of inhibition around each well were measured using a millimetre ruler. All experiments were performed in triplicates, and results were expressed as the mean ± standard deviation (SD).

2.5.2. Determination of minimum inhibitory concentration (MIC) and minimum bactericidal concentration (MBC). The MIC and MBC of Zn-BTC MOF against bacterial strains were determined using the broth microdilution method as per standard protocols.[23] Serial dilutions of the Zn-BTC MOF stock solution were prepared to obtain a concentration range of 0.02 to 0.8 mg mL^{-1}. Fresh bacterial inocula (~10^5 CFU mL^{-1}, OD_{600} = 0.03–0.05) were added to each well containing Mueller-Hinton Broth (MHB) with different concentrations of the test sample. Wells with bacterial culture but no Zn-BTC MOF served as positive controls, while MHB alone was used as the negative control. After 24 hours of incubation at 37 °C, MIC was identified as the lowest concentration at which no visible turbidity was observed. For MBC determination, samples showing no turbidity were sub-cultured on MHA plates to assess bacterial viability. Cell density was also quantified by measuring absorbance at 600 nm using a UV-Vis spectrophotometer, and values were compared to controls to confirm the inhibitory and bactericidal effects.

3. Results and discussion

3.1. Characterization

3.1.1. X-ray diffraction (XRD) analysis. The crystalline structure and phase composition of the synthesized Zn-BTC MOF were analyzed using powder X-ray diffraction (XRD) technique. As shown in Fig. 1(a), the diffraction pattern displays a series of sharp and distinct peaks in the 2θ range of 5°–40°, confirming the high crystallinity of the material. A dominant peak at 2θ = 10.1° was observed, corresponding to the characteristic reflection of Zn-BTC frameworks.[25,26] Additional diffraction peaks were observed at 2θ = 15.7°, 17.8°, 26.0°, 27.1°, 29.9°, 37.1°, and 40.8°, corresponding to higher-order reflections of the Zn-BTC structure. While the overall peak positions and patterns align well with those reported in the literature, slight shifts in peak positions and variations in relative intensities were observed. These differences may arise from minor variations in solvothermal synthesis conditions or the use of battery-derived zinc as a precursor; however, this remains a hypothesis that would require further investigation through detailed structural analysis and defect characterization.[26–28]

3.1.2. Fourier transform infrared (FTIR) spectroscopic analysis. FTIR spectroscopy was employed to investigate the functional groups present in the synthesized Zn-BTC metal–organic framework. The FTIR spectrum of Zn-BTC (Fig. 1(b))

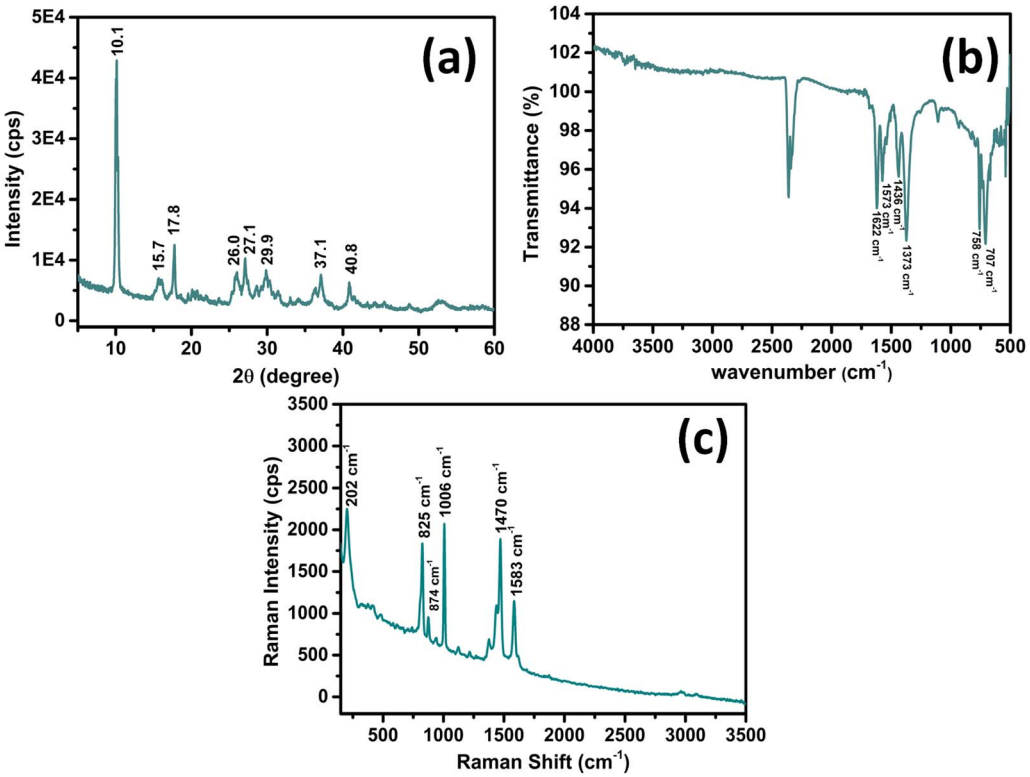

Fig. 1 (a) XRD spectrum, (b) FTIR spectrum, and (c) Raman spectrum of Zn-BTC MOF.

reveals characteristic vibrational bands that confirm the coordination between zinc ions and BTC ligands. The broad absorption band observed around 3400 cm^{-1} corresponds to the O–H stretching vibrations,[29] indicating the presence of adsorbed water molecules or uncoordinated –OH groups within the framework. The bands at 1622 cm^{-1} and 1573 cm^{-1} can be attributed to the asymmetric stretching vibration of coordinated carboxylate groups ($–COO^{–}$) bonded to Zn^{2+}, while corresponding symmetric stretching band appears around 1373 cm^{-1} and 1436 cm^{-1}, confirming successful deprotonation and coordination of the carboxylate moieties to zinc centers.[30] Band position at 1109 cm^{-1} can be attributed to the C–O stretching or in-plane bending modes of the aromatic ring or coordinated carboxylate, typical for metal–carboxylate frameworks.[31]

The peaks in the region of 600–800 cm^{-1} are associated with Zn–O stretching vibrations, which further substantiate the formation of metal–oxygen coordination bonds. The absence of a significant peak around 1700 cm^{-1}, typically ascribed to the free carboxylic acid C=O stretching, suggests complete complexation of the BTC ligand with Zn^{2+} ions. These spectral features collectively support the successful synthesis of Zn-BTC with a coordinated framework structure.

3.1.3. Raman spectroscopic analysis. Raman spectroscopy was used to investigate the structural features and coordination environment in the synthesized Zn-BTC MOF. The Raman spectrum (Fig. 1(c)) displays multiple sharp bands, confirming the vibrational modes associated with both the BTC ligand and Zn–O coordination. A low-frequency band observed at ~200 cm^{-1} is attributed to Zn–O stretching vibrations, indicating successful metal–ligand coordination in the framework. The peaks at 825 cm^{-1} and 874 cm^{-1} correspond to C–H out-of-plane bending modes of the aromatic benzene ring from the BTC ligand.[32] A prominent band at 1006 cm^{-1} is assigned to the symmetric ring breathing mode of the benzene ring, which is characteristic of aromatic carboxylate ligands.[33] The peaks at 1470 cm^{-1} and 1583 cm^{-1} represent the symmetric and asymmetric stretching vibrations of C=C bonds in the aromatic system, confirming the intact nature of the BTC structure after MOF formation.[34]

3.1.4. Field emission scanning electron microscopy (FESEM) and energy dispersive X-ray spectroscopic (EDX) analysis. The morphology and particle size distribution of Zn-BTC MOF were investigated using FESEM analysis. As shown in Fig. 2(a and b), particles of Zn-BTC exhibit a densely packed, aggregated morphology composed of irregularly shaped nanoparticles. The nanoscale dimensions of the particles are evident, with no apparent large crystallites or macroscopic agglomeration, suggesting uniform nucleation during synthesis.[35] Image analysis of over 75 particles (Fig. 2(c)) revealed an average particle size of 51.50 ± 21.71 nm, indicating nanometric scale which is favourable for electrochemical applications due to enhanced surface-to-volume ratio and diffusion properties. Elemental composition was assessed through EDX spectroscopy (Fig. 2(d)), which confirms the presence of carbon (C), oxygen (O), and zinc (Zn) as the primary elements. The quantification yielded atomic percentages of C:

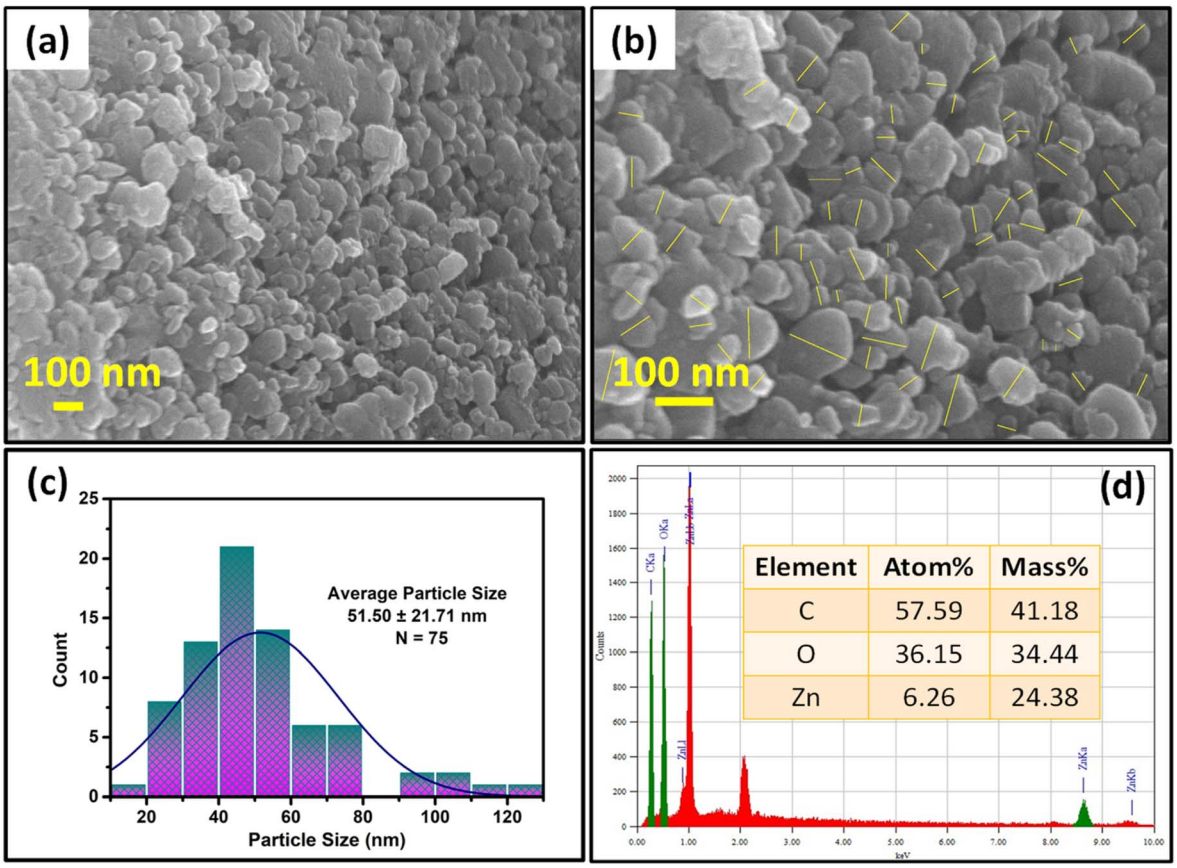

Fig. 2 (a) and (b) FESEM images, (c) particle size distribution histogram, and (d) EDX spectrum with elemental composition of Zn-BTC MOF.

57.59%, O: 36.15%, and Zn: 6.26%, with respective mass contributions of 41.18%, 34.44%, and 24.38%.

3.1.5. Transmission electron microscopy (TEM) and elemental analysis. The internal morphology, crystallinity, and particle size distribution of Zn-BTC were examined using TEM. Fig. 3(a–c) depict low- and high-magnification TEM images, revealing aggregated, nearly spherical nanoparticles with smooth boundaries. Particle size distribution analysis (Fig. 3(d)) of 15 particles reveals an average size of 44.84 ± 12.50 nm, corroborating FESEM measurements and affirming nanoscale dimensions. High-resolution TEM (HRTEM) (Fig. 3(c)) highlights clear lattice fringes, indicating crystalline order within individual particles, while the selected area electron diffraction (SAED) pattern (Fig. 3(e)) displays concentric rings, confirming the polycrystalline nature of the Zn-BTC structure.[36] The EDS spectrum (Fig. 3(f)) identifies C, O and Zn. The observed Cu signal, which dominates the spectrum (20.98%), originates from the copper TEM grid, while Zn is present in low detectable concentration (0.03%), typical for MOFs due to their organic-rich composition. The atomic percentages of C: 75.12% and O: 3.87% are consistent with the organic BTC ligand and framework oxygen atoms.

3.1.6. X-ray photoelectron spectroscopic (XPS) analysis. XPS analysis was conducted to investigate the surface elemental composition and chemical states of the elements in Zn-BTC. The wide survey spectrum (Fig. 4(a)) confirms the presence of Zn, O, and C, with prominent peaks corresponding to Zn 2p, O 1s, and C 1s orbitals. The high-resolution spectrum of Zn 2p (Fig. 4(b)) displays two intense peaks at approximately 1022.2 eV and 1045.3 eV, which can be assigned to Zn $2p_{3/2}$ and Zn $2p_{1/2}$, respectively.[37] The binding energy of the Zn $2p_{3/2}$ peak at 1022.2 eV indicates the divalent oxidation state of zinc (Zn^{2+}), consistent with Zn coordinated to carboxylate ligands in the BTC framework. The spin orbit splitting of about 23.1 eV confirms the presence of Zn. In the O 1s spectrum (Fig. 4(c)), a dominant peak at around 532.4 eV is attributed to oxygen in carboxylate groups ($-COO^-$), while minor contributions from hydroxyl groups and adsorbed water appear at slightly higher binding energies.[38] This suggests the successful binding of BTC's oxygen atoms with Zn^{2+} centre. The deconvoluted C 1s spectrum (Fig. 4(d)) reveals three main components: a peak at 284.6 eV corresponding to C–C/C=C bonds from the aromatic BTC ring, a peak at 286.3 eV associated with C–O functionalities, and a higher binding energy peak at 288.9 eV representing O–C=O species from carboxylic groups.[39] These features corroborate the integration of BTC ligands in the MOF structure through carboxylate coordination.

3.1.7. Thermogravimetric and differential scanning calorimetry (TG-DSC) analysis. The thermal stability and decomposition behaviour of Zn-BTC were evaluated using simultaneous TG-DSC analysis (Fig. 5). The thermogram reveals multiple stages of mass loss, corresponding to the release of

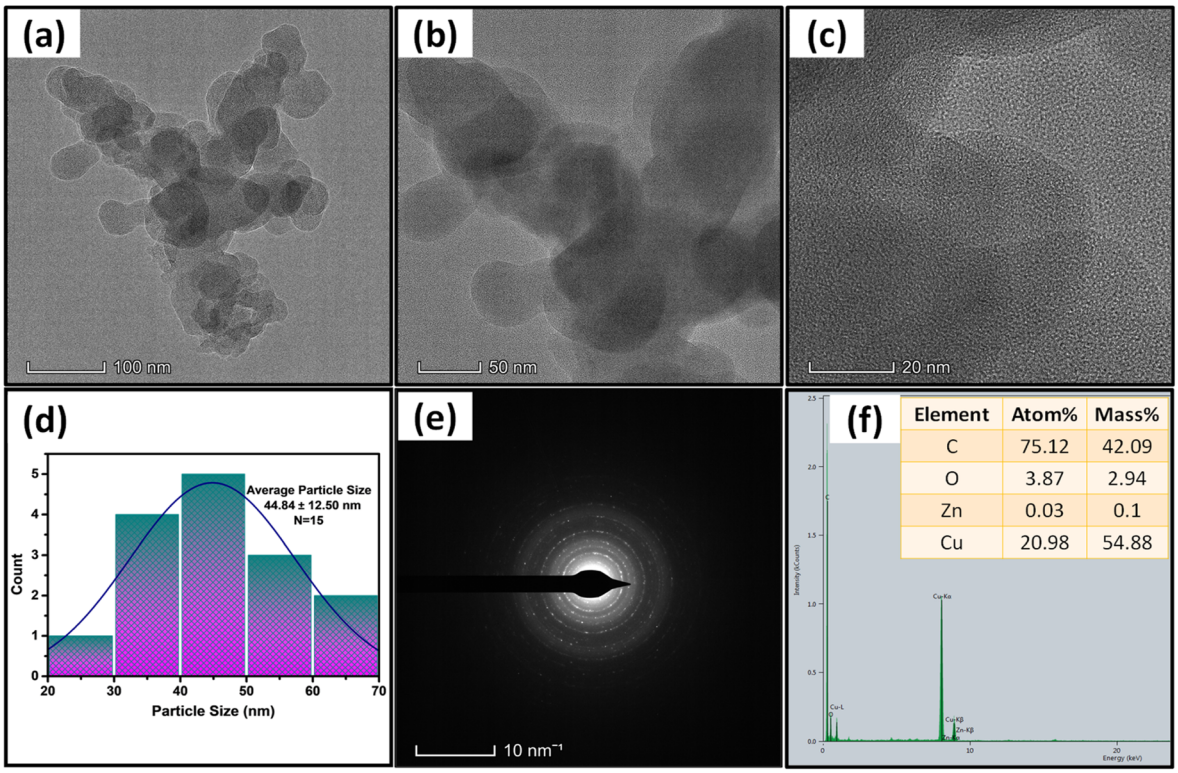

Fig. 3 (a)–(c) TEM images, (d) particle size distribution histogram, (e) SAED pattern, and (f) EDS spectrum with elemental composition.

physisorbed water, coordinated solvent molecules, and framework decomposition. The initial mass loss of approximately 0.67% below 150 °C corresponds to the removal of adsorbed moisture, with a small endothermic DSC peak indicating evaporation. The second stage, occurring between 200–450 °C, accounts for a more significant weight loss of about 38.83%, attributed to the decomposition of organic BTC linkers. This region features exothermic events with enthalpic values of -34.47 J g^{-1}, -2.934 J g^{-1}, and -55.34 J g^{-1}, signifying structural breakdown and combustion of organic constituents. A final broad endothermic transition between 500–750 °C is observed in the DSC curve, with an associated energy of 222.3 J g^{-1}, which likely corresponds to further degradation of carbonaceous residues and stabilization of the resulting inorganic phase. At 800 °C, the material retains a residual mass of 46.55%, which suggests the formation of thermally stable ZnO or inorganic metal oxide residue after framework decomposition. This analysis affirms that Zn-BTC is thermally stable up to approximately 400 °C, making it a viable candidate for electrochemical and biological applications within moderate thermal environments.

3.2. Electrochemical analysis

3.2.1. Electrocatalytic activity of Zn-BTC MOF toward UA. Fig. 6(a) shows the CV curves of the Zn-BTC/GCE in the presence and absence of 100 μM UA over a potential range of -0.5 to +1.0 V at a scan rate of 50 mV s^{-1}. A significant increase in the anodic current was observed in the presence of UA, confirming the enhanced electrocatalytic activity of the MOF. A well-defined oxidation peak appeared near +0.55 V, corresponding to UA oxidation. This is attributed to the increased surface area and active sites available on the Zn-BTC framework, which facilitate faster electron transfer.[40] In contrast, the bare GCE showed only a weak and broad oxidation signal, reflecting poor catalytic behaviour. The Zn-BTC MOF layer reduced the oxidation overpotential, implying faster redox kinetics and improved UA adsorption.

3.2.2. Concentration dependent response and sensitivity. The concentration-dependent electrocatalytic response of the Zn-BTC/GCE was further evaluated using CV for UA concentrations ranging from 0 to 300 μM (Fig. 6(b)). A systematic increase in anodic peak current was observed with increasing UA concentrations, with no substantial peak shift, indicating a stable catalytic process. The corresponding calibration curve is shown in Fig. 6(c), which reveals a linear relationship ($R^2 = 0.9882$) between peak current and UA concentration from 0 to 200 μM. The linear regression equation is presented as follows.

$$i_{PC} = 0.0087C_{UA} + 3.7497 \quad (1)$$

where i_{PC} is the anodic peak current (μA) and C_{UA} is the UA concentration (μM). The limit of detection (LOD) can be calculated using the formula as given below.

$$\mathrm{LOD} = \frac{3\sigma}{S} \quad (2)$$

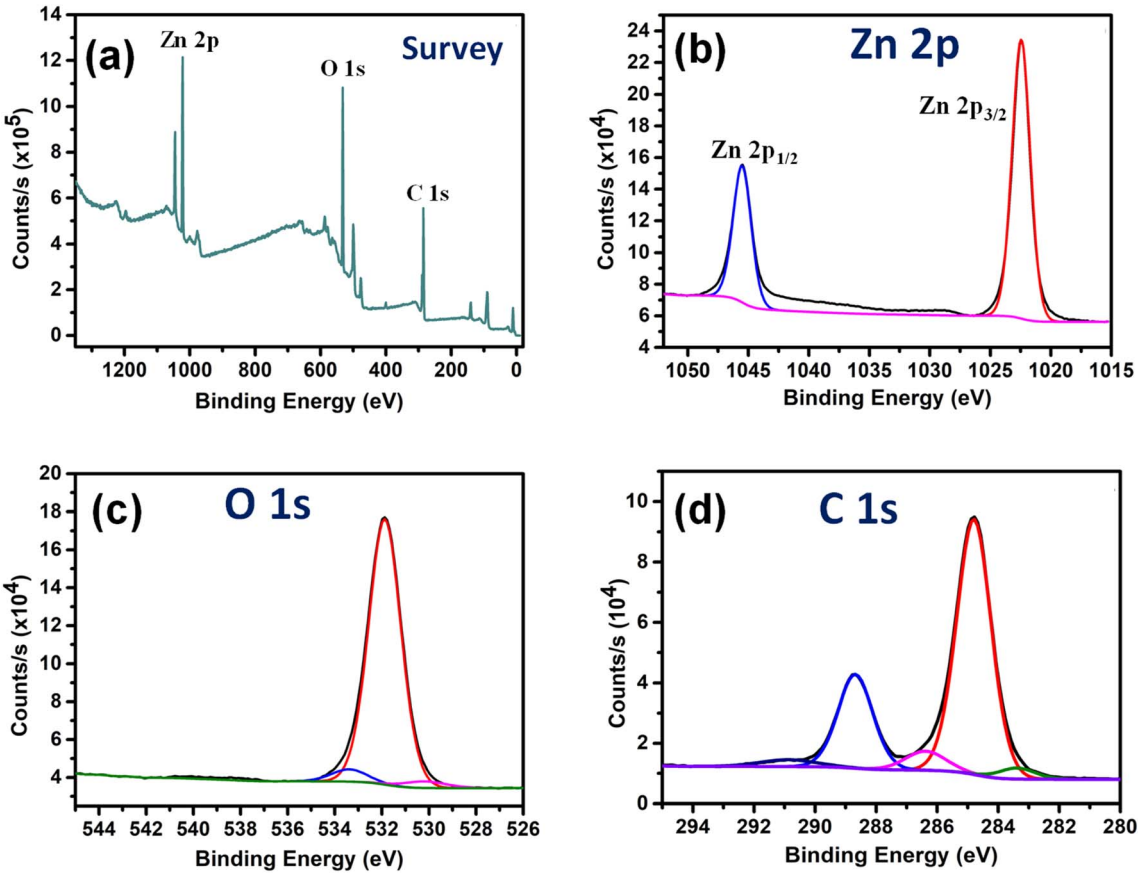

Fig. 4 XPS analysis of Zn-BTC MOF: (a) survey spectra; high resolution spectra of (b) Zn 2p, (c) O 1s and (d) C 1s.

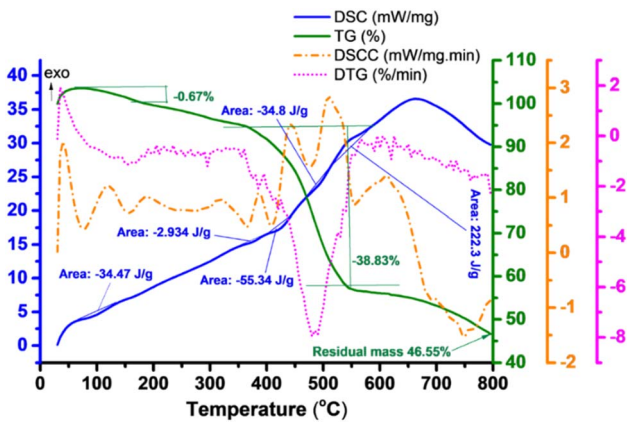

Fig. 5 Simultaneous thermal analysis of Zn-BTC MOF showing thermogravimetric (TG), differential scanning calorimetry (DSC), derivative thermogravimetry (DTG), and differential scanning calorimetric capacity (DSCC) curves.

where σ is the standard deviation of the blank response and S is the slope of the calibration curve. Using a slope of 0.00867 μA μM^{-1} and a standard deviation of 0.003761, the LOD was estimated to be 1.43 μM, indicating the sensor's suitability for detecting UA at physiologically relevant levels.

3.2.3. Scan rate study and kinetics. To understand the redox kinetics, CVs were recorded at various scan rates from 10 to 100 mV s^{-1} (Fig. 6(d)). The peak currents increased with scan rate, and the redox peaks remained well defined. When the peak current (i_{PC}) was plotted against scan rate (v), a linear relationship ($R^2 = 0.9811$) was observed (Fig. 6(e)), indicating that the oxidation process is adsorption-controlled at higher scan rates. The obtained linear equation is presented as follows.

$$i_{PC} = 0.0531v + 0.7913 \quad (3)$$

To further examine the mechanism, peak currents were plotted against the square root of scan rate ($v^{1/2}$). As shown in Fig. 6(f), the anodic and cathodic peak currents exhibited linear relationship ($R^2 = 0.99$ for both case) with $v^{1/2}$. The corresponding anodic and cathodic equations are presented respectively as follows.

$$i_{Pa} = 0.7236v^{1/2} + 0.9719 \quad (4)$$

$$i_{Pc} = -0.6738v^{1/2} - 1.4288 \quad (5)$$

This confirms that the redox process is also diffusion-controlled, especially at lower scan rates. The presence of both relationships ($i \propto v$ and $i \propto v^{1/2}$) indicates a mixed kinetic regime involving both adsorption-controlled and diffusion-

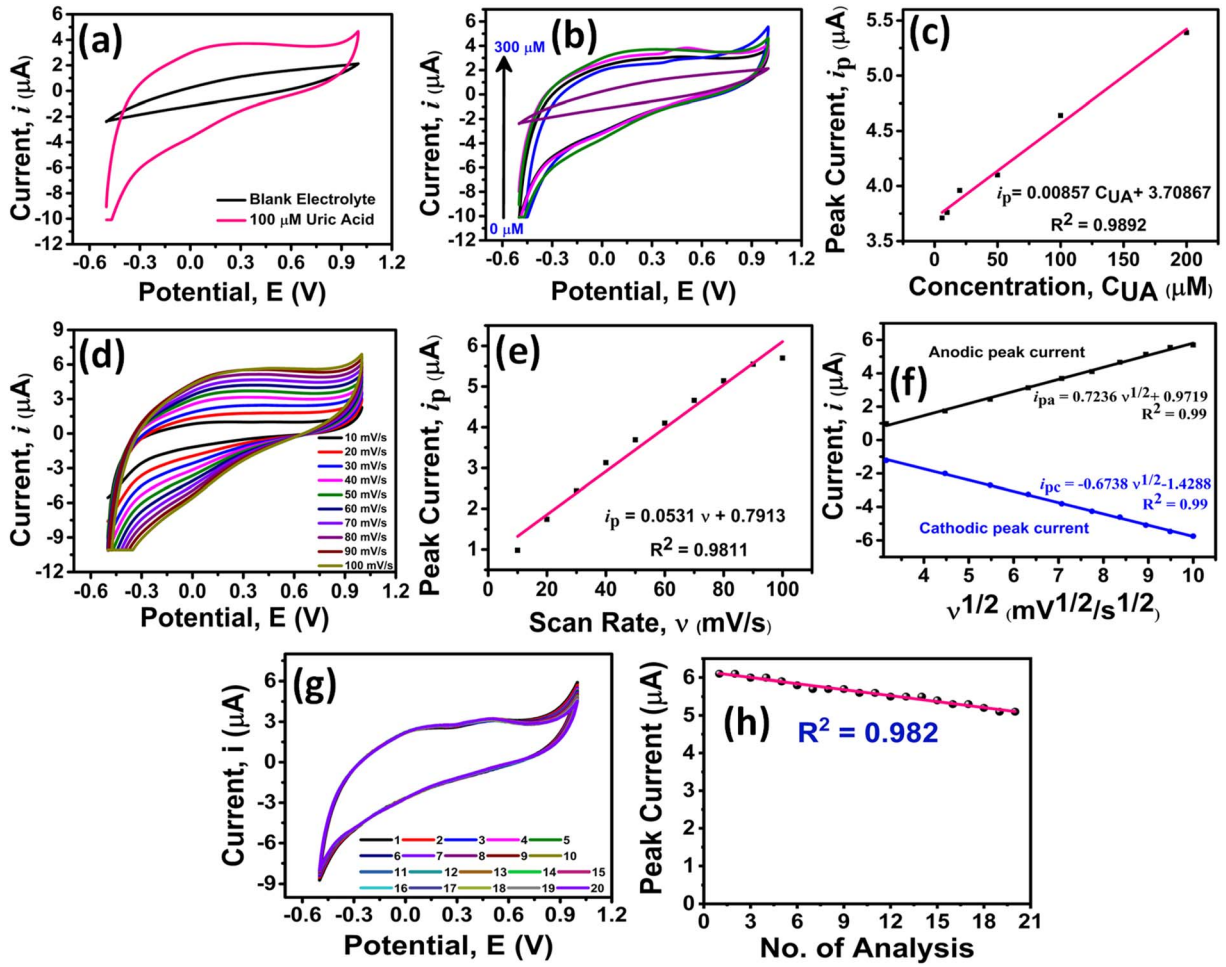

Fig. 6 Electrochemical sensing of UA by using Zn-BTC/GCE as working electrode: (a) current, *i vs.* potential, *E* curves for blank electrolyte and 100 μM UA at 50 mV s^{-1} scan rate, (b) *i vs. E* curves for 0–300 μM UA solutions at 50 mV s^{-1} scan rate, (c) peak current *vs.* concentration of UA plot (d) *i vs. E* curves for 100 μM UA solutions at 10–100 mV s^{-1}, (e) *i vs.* ν plot, (f) *i vs.* $\nu^{1/2}$ plot, (g) *i vs. E* curves for 20 consecutive CV scans recorded at Zn-BTC/GCE in 100 μM uric acid (0.1 M PBS, scan rate = 50 mV s^{-1}), and (h) linear fitted plot of peak current *vs.* cycle number. The electrode retained 83.33% of the initial peak current after 20 cycles (RSD = 7.89%).

Table 1 Comparative study of different material modified GCE with Zn-BTC/GCE for uric acid sensing

Electrode material	Linear range (μM)	LOD (μM)	Reference
Zn-BTC	0–200	1.43	This study
Au decorated Ni-MOF	15–500	5.6	45
Au NPs	0.5–600	0.25	46
Cu-MOF	0.5–600	0.2	47
Polypyrrole-carbon black-Co_3O_4	—	0.46	48
Polypyrrole-Fe-MOF	1–300	0.212	49

controlled processes. This dual kinetic regime indicates that the electrochemical oxidation of UA at the Zn-BTC MOF-modified electrode involves both surface adsorption and mass transport mechanisms. Such behaviour is advantageous for sensing applications, as it ensures fast electron transfer (adsorption-dominated) and accessibility of the analyte even at lower concentrations (diffusion-dominated). This observed mixed kinetic control can be rationalized by considering the structural characteristics of the Zn-BTC MOF. The presence of abundant active Zn sites coordinated with carboxylate groups facilitates strong adsorption of uric acid molecules onto the electrode surface, thus contributing to the adsorption-controlled process at higher scan rates.[41] Furthermore, the nanoscale morphology and interconnected pore channels inherent to the MOF architecture can enhance the accessibility of analytes, enabling efficient diffusion of UA from the bulk solution toward the electrode surface.[42] The high surface area of the Zn-BTC/GCE provides numerous adsorption sites, while the porosity reduces mass transfer limitations, resulting in rapid analyte transport.[43] Together, these structural factors promote a dual kinetic regime where adsorption dominates at higher scan rates due to surface interactions, whereas diffusion governs the process at lower scan rates where mass transport from the bulk solution is critical. This combination of adsorption-driven electron transfer and diffusion-assisted analyte supply ultimately enhances the sensor's sensitivity and responsiveness.

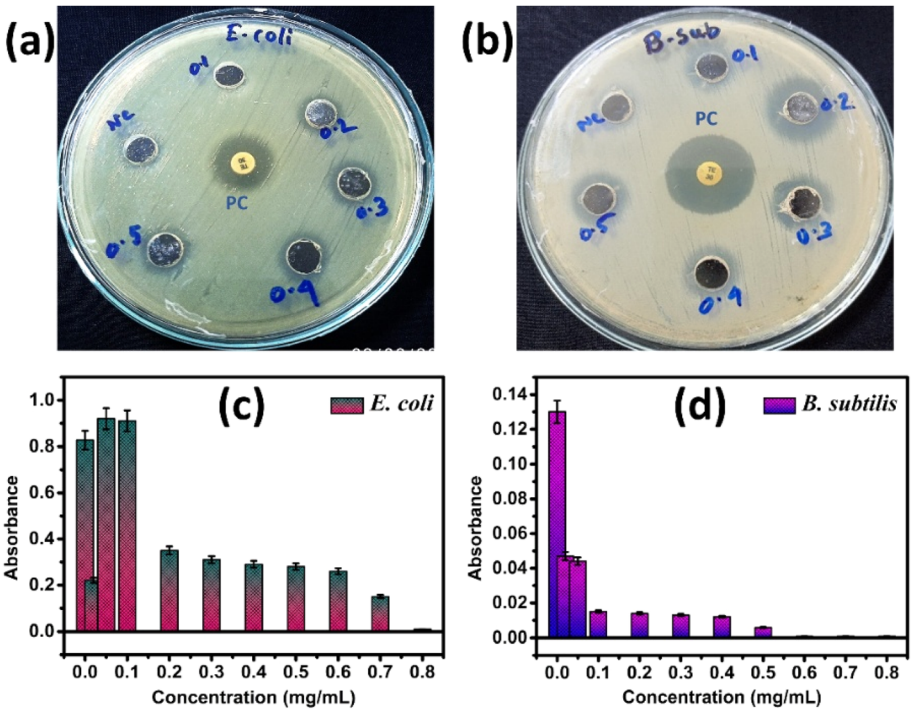

Fig. 7 Antibacterial activity of Zn-BTC MOF against (a) *Escherichia coli* and (b) *Bacillus subtilis* at different concentrations where PC refers to positive control and NC refers to negative control; evaluation of minimum inhibitory concentration (MIC) and minimum bactericidal concentration (MBC) against (c) *Escherichia coli*, and (d) *Bacillus subtilis*.

3.2.4. Electroactive surface area estimation. The electrochemically active surface area (A) of the Zn-BTC/GCE was estimated using the Randles–Sevcik equation as presented below.

$$i_P = (2.69 \times 10^5) n^{3/2} A D^{1/2} C_{UA} v^{1/2} \quad (6)$$

where, $n = 2$ (number of electrons transferred), A = electroactive surface area (cm^2), D = diffusion coefficient of UA (5.5×10^{-6} cm^2 s^{-1}), C_{UA} = concentration of UA (100 μM or 1.0×10^{-4} mol L^{-1}).

From the slope of the i_p *versus* $v^{1/2}$ plot and applying this equation, the electroactive surface area of Zn-BTC/GCE was calculated to be 0.16 cm^2, which is significantly larger than that of the bare GCE (~0.071 cm^2). This confirms that the Zn-BTC MOF contributes significantly to increasing the active surface area and hence the electrocatalytic response.

3.2.5. Cycling stability assessment. The cycling stability of the Zn-BTC/GCE was evaluated by recording twenty consecutive cyclic voltammograms in 100 μM uric acid prepared in 0.1 M PBS (pH 7.4) at a scan rate of 50 mV s^{-1} (Fig. 6(g)). The Zn-BTC/

Table 2 Results of antibacterial activity of Zn-BTC MOF by agar well diffusion assay. Tetracycline disc was used as positive control and DMSO solvent as negative control[a]

		Zone of inhibition in cm	
		Gram positive bacteria	Gram negative bacteria
		B. subtilis	*E. coli*
Sample	Concentration	*ATCC 6633*	*ATCC 11229*
Zn-BTC MOF	0.1 mg mL^{-1}	1.3 ± 0.15	—
	0.2 mg mL^{-1}	**2.0 ±0.18**	1.3 ± 0.50
	0.3 mg mL^{-1}	1.5 ± 0.22	**1.5 ±0.17**
	0.4 mg mL^{-1}	1.4 ± 0.16	1.3 ± 0.26
	0.5 mg mL^{-1}	1.7 ± 0.25	1.2 ± 0.21
Positive control	30 μg	3.1 ± 0.16	1.8 ± 0.50
Negative control	—	—	—

[a] "—" indicates no zone of inhibition.

GCE exhibited variation in peak current in the repeated measurements where 16.67% decrease in oxidation peak current was observed after the 20th cycle compared to the first. The relative standard deviation (RSD) of the peak current responses was calculated to be 7.89%. The observed decrease in peak current reflects the possibility of incidences such as minor surface fouling, partial detachment or restructuring of the MOF film, or slight Zn leaching under repeated oxidative scans.[44]

3.2.6. Comparison of Zn-BTC/GCE with existing works. A comparative study was conducted to evaluate the performance of our Zn-BTC MOF GCE for uric acid (UA) sensing against other modified electrodes. Table 1 presents the linear range and limit of detection (LOD) for UA sensing using these various modified electrodes.

3.3. Antibacterial activity of Zn-BTC MOF

The antibacterial potential of Zn-BTC MOF was investigated at different concentrations against *Escherichia coli* and *Bacillus subtilis* using the agar well diffusion method (Fig. 7(a and b)). As shown in Table 2, Zn-BTC MOF demonstrated dose-dependent inhibition of bacterial growth. The largest inhibition zone against *B. subtilis* was observed at 0.2 mg mL^{-1} (2.0 $\pm$ 0.18 cm), whereas *E. coli* showed its highest response at 0.3 mg mL^{-1} (1.5 $\pm$ 0.17 cm). The positive control (tetracycline disc) showed significant inhibition against both strains, whereas the negative control (DMSO) exhibited no inhibitory effect.

To further determine the inhibitory and bactericidal concentrations, MIC and MBC values were calculated using broth microdilution assays. For *E. coli*, the MIC was found to be 0.2 mg mL^{-1}, while the MBC was 0.8 mg mL^{-1} (Fig. 7(c)). In the case of *B. subtilis*, Zn-BTC MOF showed greater sensitivity with a MIC of 0.1 mg mL^{-1} and MBC of 0.6 mg mL^{-1} (Fig. 7(d)). These findings indicate that Zn-BTC MOF is more effective against *B. subtilis* than *E. coli*, likely due to structural differences in the cell walls of Gram-positive and Gram-negative bacteria. The antibacterial activity of Zn-BTC MOF is likely attributed to a mechanism commonly reported for Zn-based MOFs, where gradual Zn^{2+} ion release from the framework can disrupt bacterial membranes and interfere with enzymatic processes, leading to cell death. However, it should be noted that the present study did not directly measure Zn^{2+} release or its interaction with bacterial membranes; thus, this mechanism is proposed based on literature and warrants further experimental confirmation.[20]

According to previous reports, under physiological or mildly acidic conditions (*e.g.* infection microenvironment, pH ~5.5), partial hydrolysis of the Zn–BTC coordination bonds induces controlled Zn^{2+} ion release, which disrupts bacterial membranes and enzymatic function, particularly in Gram-positive *B. subtilis* and Gram-negative *E. coli*.[50] The nanoscale morphology enhances surface contact with bacteria, increasing local Zn^{2+} concentrations and promoting bactericidal efficiency. *In vivo* studies of previous reports show that Zn-BTC MOF also supports wound healing and exhibits anti-inflammatory effects *via* sustained zinc release and low cytotoxicity.[50]

Regarding the electrochemical sensing, the enhanced electrochemical sensing performance of Zn-BTC MOF toward uric acid can be principally attributed to its crystalline architecture and nanoscale morphology. The highly ordered framework, as confirmed by XRD and TEM, provides an organized array of Zn nodes linked by BTC units, which facilitates effective electron transport. Nanoscale dimensions observed in FESEM and TEM further depicts an increased electroactive surface area which enables more uric acid molecules to access the redox-active sites.[50,51]

4. Conclusion

In this work, a sustainable and cost-effective approach for the synthesis of a zinc-based metal–organic framework was demonstrated by utilizing zinc, recovered from waste dry cell batteries. The synthesis involved extraction, hydroxide precipitation, and coordination with BTC under mild solvothermal conditions, yielding a crystalline, thermally stable, and nanostructured MOF. Comprehensive characterization using XRD, FTIR, Raman, SEM, TEM, XPS, and TGA confirmed the formation of a pure, porous, and structurally robust Zn-BTC framework. The material exhibited significant electrocatalytic activity toward the oxidation of uric acid, with a wide linear detection range, low detection limit, and high electroactive surface area. Scan rate studies further revealed a mixed kinetic control, combining both adsorption and diffusion-driven processes. In addition to sensing performance, Zn-BTC MOF showed promising antibacterial activity. The material effectively inhibited the growth of both Gram-positive and Gram-negative bacteria, with lower MIC and MBC values against *B. subtilis*. The dual functionality (electrochemical and antimicrobial) highlights the versatility of Zn-BTC MOF for biomedical and environmental applications. The integration of waste-derived synthesis with dual functional performance positions this study at the intersection of sustainability and practical material innovation. By demonstrating that high-value MOFs can be fabricated from electronic waste, this work contributes toward greener synthesis protocols and supports a more circular approach to materials science.

Author contributions

Md Sohag Hossain: conceptualization, methodology, investigation, data curation, writing – original draft. Sharuk Alam Aumi: methodology, investigation, data curation, writing – original draft. Nourin Tarannum: methodology, investigation, data curation, writing – original draft. Fariha Chowdhury: formal analysis, investigation, data curation. Md. Sahadat Hossain: formal analysis. Md. Farid Ahmed: formal analysis. Nazmul Islam Tanvir: formal analysis. Umme Sarmeen Akhtar: formal analysis, investigation, data curation. Samina Ahmed: supervision, resources. Mashrafi Bin Mobarak: conceptualization, supervision, funding acquisition, project administration, writing – review & editing.

Conflicts of interest

There is no conflict to declare.

Data availability

All data supporting the findings of this study are included in the main manuscript. Raw data are available from the corresponding author (mashrafibinmobarak@gmail.com) upon reasonable request.

Acknowledgements

The authors gratefully acknowledge the Bangladesh Council of Scientific and Industrial Research (BCSIR) for providing essential support for this research through its R&D project initiative for FY 2025-26. We also appreciate the unwavering support from Semiconductor Technology Research Centre (STRC) and Physical Chemistry Research Laboratory, Department of Chemistry, University of Dhaka.

References

1 S. A. Fathallah-Shaykh and M. T. Cramer, *Pediatr. Nephrol.*, 2014, **29**, 999–1008.
2 D.-H. Kang, T. Nakagawa, L. Feng, S. Watanabe, L. Han, M. Mazzali, L. Truong, R. Harris and R. J. Johnson, *J. Am. Soc. Nephrol.*, 2002, **13**, 2888.
3 D. I. Feig, D.-H. Kang and R. J. Johnson, *N. Engl. J. Med.*, 2008, **359**, 1811–1821.
4 Y. Saito, A. Tanaka, K. Node and Y. Kobayashi, *J. Cardiol.*, 2021, **78**, 51–57.
5 D. Lakshmi, M. J. Whitcombe, F. Davis, P. S. Sharma and B. B. Prasad, *Electroanalysis*, 2011, **23**, 305–320.
6 Q. Wang, X. Wen and J. Kong, *Crit. Rev. Anal. Chem.*, 2020, **50**, 359–375.
7 J.-F. Jen, S.-L. Hsiao and K.-H. Liu, *Talanta*, 2002, **58**, 711–717.
8 J. C. Fanguy and C. S. Henry, *Electrophoresis*, 2002, **23**, 767–773.
9 J. Yu, L. Ge, J. Huang, S. Wang and S. Ge, *Lab Chip*, 2011, **11**, 1286–1291.
10 N. C. A. Rashid, N. H. Ngajikin, A. I. Azmi, R. Arsat, S. Isaak, N. A. Cholan and N. E. Azmi, *Chin. Opt. Lett.*, 2019, **17**, 081701.
11 J. Galbán, Y. Andreu, M. J. Almenara, S. de Marcos and J. R. Castillo, *Talanta*, 2001, **54**, 847–854.
12 E. T. S. G. da Silva, D. E. P. Souto, J. T. C. Barragan, J. de F. Giarola, A. C. M. de Moraes and L. T. Kubota, *ChemElectroChem*, 2017, **4**, 778–794.
13 P. K. Kalambate, Z. Rao, Dhanjai, J. Wu, Y. Shen, R. Boddula and Y. Huang, *Biosens. Bioelectron.*, 2020, **163**, 112270.
14 M. K. Muthukumaran, M. Govindaraj, S. Kogularasu, B. Sriram, B. K. Raja, S.-F. Wang, G.-P. Chang-Chien and A. Selvi J, *Talanta Open*, 2025, **11**, 100396.
15 B. Mohanty, S. Kumari, P. Yadav, P. Kanoo and A. Chakraborty, *Coord. Chem. Rev.*, 2024, **519**, 216102.
16 V. Stavila, A. A. Talin and M. D. Allendorf, *Chem. Soc. Rev.*, 2014, **43**, 5994–6010.
17 S. Bahrani, H. Seyyed, A. Mousavi, S. Mojtaba and R. Azhdari, *Drug Metab. Rev.*, 2019, **51**, 356–377.
18 J. Zhang, L. Gao, Y. Zhang, R. Guo and T. Hu, *Microporous Mesoporous Mater.*, 2021, **322**, 111126.
19 F.-H. Zhao, Y.-S. Li, S.-Q. Li, X.-H. Wu, Y.-C. He and Z.-L. Li, *CrystEngComm*, 2025, **27**, 2223–2232.
20 M. Nakhaei, K. Akhbari, M. Kalati and A. Phuruangrat, *Inorg. Chim. Acta*, 2021, **522**, 120353.
21 F. Akbarzadeh, M. Motaghi, N. P. S. Chauhan and G. Sargazi, *Heliyon*, 2020, **6**, e03231.
22 J.-H. Wang, F. Kong, B.-F. Liu, N.-Q. Ren and H.-Y. Ren, *Coord. Chem. Rev.*, 2025, **533**, 216534.
23 M100 | Performance Standards for Antimicrobial Susceptibility Testing, **https://clsi.org/shop/standards/m100/**, accessed July 1, 2025.
24 F. D. Gonelimali, J. Lin, W. Miao, J. Xuan, F. Charles, M. Chen and S. R. Hatab, *Front. Microbiol.*, 2018, **9**, 1639.
25 X. Wang, X. Ma, H. Wang, P. Huang, X. Du and X. Lu, *Microchim. Acta*, 2017, **184**, 3681–3687.
26 H. Deepika, M. Kaur, K. Singh Dhaliwal, H. Kaur and A. Kumar Malik, *J. Fluoresc.*, 2022, **32**, 1565–1580.
27 N. Bhardwaj, S. K. Pandey, J. Mehta, S. K. Bhardwaj, K.-H. Kim and A. Deep, *Toxicol. Res.*, 2018, **7**, 931–941.
28 L. Aftab, N. Iqbal, A. Asghar and T. Noor, *Sep. Sci. Technol.*, 2021, **56**, 2159–2169.
29 M. Asadi, B. Babamiri, R. Hallaj and A. Salimi, *J. Electroanal. Chem.*, 2022, **914**, 116306.
30 R. D. Webster, *J. Chem. Soc., Perkin Trans. 2*, 2002, 1882–1888.
31 M. F. M. Fadli, H. Misran, S. Z. Othman, A. M. S. Bahari, N. A. Samsudin, S. A. Rosli, Z. Lockman, A. Matsumoto and N. Amin, *International Journal of Recent Technology and Engineering*, 2019, **8**, 6490–6498.
32 M. Margoshes and V. A. Fassel, *Spectrochim. Acta*, 1955, **7**, 14–24.
33 R. T. Ulahannan, C. Y. Panicker, H. T. Varghese, R. Musiol, J. Jampilek, C. V. Alsenoy, J. A. War and T. K. Manojkumar, *Spectrochim. Acta, Part A*, 2015, **150**, 190–199.
34 G. Socrates, *Infrared and Raman Characteristic Group Frequencies: Tables and Charts*, John Wiley & Sons, 2004.
35 S. Jabarian and A. Ghaffarinejad, *New J. Chem.*, 2020, **44**, 19820–19826.
36 L. Yue, L. Chen, X. Wang, D. Lu, W. Zhou, D. Shen, Q. Yang, S. Xiao and Y. Li, *Chem. Eng. J.*, 2023, **451**, 138687.
37 X. Li, L. Liu, C. Tu, Q. Zhang, X. Yang, D. I. Kolokolov, H. Maltanava, N. Belko, S. Poznyak, M. Samtsov, H. Guo, S. Wu and M. Zhu, *Nanomaterials*, 2024, **14**, 22.
38 Z. Wang, J. Xu, J. Yang, Y. Xue and L. Dai, *Chem. Eng. J.*, 2022, **427**, 131498.
39 L. Pan, T. Muhammad, L. Ma, Z.-F. Huang, S. Wang, L. Wang, J.-J. Zou and X. Zhang, *Appl. Catal., B*, 2016, **189**, 181–191.
40 L. Liu, L. Liu, Y. Wang and B.-C. Ye, *Talanta*, 2019, **199**, 478–484.

41 A. Sarkar, A. Adhikary, A. Mandal, T. Chakraborty and D. Das, *Cryst. Growth Des.*, 2020, **20**, 7833–7839.
42 H. Furukawa, K. E. Cordova, M. O'Keeffe and O. M. Yaghi, *Science*, 2013, **341**, 1230444.
43 S. Tajik, H. Beitollahi, F. G. Nejad, K. O. Kirlikovali, Q. Van Le, H. W. Jang, R. S. Varma, O. K. Farha and M. Shokouhimehr, *Cryst. Growth Des.*, 2020, **20**, 7034–7064.
44 B. D. McCarthy, A. M. Beiler, B. A. Johnson, T. Liseev, A. T. Castner and S. Ott, *Coord. Chem. Rev.*, 2020, **406**, 213137.
45 F. Li, L. Liu, T. Liu and M. Zhang, *Ionics*, 2022, **28**, 4843–4851.
46 N. Stozhko, M. Bukharinova, L. Galperin and K. Brainina, *Biosensors*, 2018, **8**, 21.
47 Q. Azizpour Moallem and H. Beitollahi, *Microchem. J.*, 2022, **177**, 107261.
48 J. Ahmed, M. Faisal, S. A. Alsareii and F. A. Harraz, *Adv. Compos. Hybrid Mater.*, 2022, **5**, 920–933.
49 R. Wang, Y. Zhu, S. Liu, K. Jiang, R. Wang, S. Ji, M. Ma, Q. Chen, H. Ran and X. Song, *Microchem. J.*, 2025, **212**, 113441.
50 Y. Chen, J. Cai, D. Liu, S. Liu, D. Lei, L. Zheng, Q. Wei and M. Gao, *Regener. Biomater.*, 2022, **9**, rbac019.
51 S. Sadeghi and J. Javanshiri-Ghasemabadi, *RSC Adv.*, 2024, **14**(11), 7836–7849.